

Coordinated Multiwavelength Observations of 3C 66A during the WEBT campaign of 2003 – 2004¹

M. Böttcher¹, J. Harvey¹, M. Joshi¹, M. Villata², C. M. Raiteri², D. Bramel³, R. Mukherjee³, T. Savolainen⁶, W. Cui⁵, G. Fossati⁴, I. A. Smith⁴, D. Able⁵, H. D. Aller⁷, M. F. Aller⁷, A. A. Arkharov⁸, K. Baliyan³⁴, D. Barnaby⁹, A. Berdyugin⁶, E. Benítez¹⁴, P. Boltwood¹⁰, M. Carini⁹, D. Carosati¹¹, S. Ciprini¹², J. M. Coloma¹³, S. Crapanzano², J. A. de Diego¹⁴, A. Di Paola⁴⁰, M. Dolci⁴¹, J. Fan¹⁵, A. Frasca¹⁶, V. Hagen-Thorn^{17,18}, D. Horan³⁷, M. Ibrahimov^{19,20}, G. N. Kimeridze²¹, Y. A. Kovalev³⁶, Y. Y. Kovalev^{36,42}, O. Kurtanidze²¹, A. Lähteenmäki²⁹, L. Lanteri², V. M. Larionov^{17,18}, E. G. Larionova¹⁷, E. Lindfors⁶, E. Marilli¹⁶, N. Mirabal²², M. Nikolashvili²¹, K. Nilsson⁶, J. M. Ohlert²³, T. Ohnishi²⁴, A. Oksanen²⁵, L. Ostorero^{6,39}, G. Oye³⁵, I. Papadakis^{26,27}, M. Pasanen⁶, C. Poteet⁹, T. Pursimo³⁵, K. Sadakane²⁴, L. A. Sigua²¹, L. Takalo⁶, J. B. Tartar²⁸, H. Teräsrananta²⁹, G. Tosti¹², R. Walters⁹, K. Wiik^{6,38}, B. A. Wilking²⁸, W. Wills⁹, E. Xilouris³⁰, A. B. Fletcher³¹, M. Gu^{31,32,33}, C.-U. Lee³¹, S. Pak³¹, H.-S. Yim³¹

ABSTRACT

The BL Lac object 3C 66A was the target of an extensive multiwavelength monitoring campaign from July 2003 through April 2004 (with a core campaign from Sept. – Dec. 2003), involving observations throughout the electromagnetic spectrum. Radio, infrared, and optical observations were carried out by the WEBT-ENIGMA collaboration. At higher energies, 3C 66A was observed in X-rays (RXTE), and at very-high-energy (VHE) γ -rays (STACEE, VERITAS). In addition, the source has been observed with the VLBA at 9 epochs throughout the period September 2003 – December 2004, including 3 epochs contemporaneous with the core campaign.

A gradual brightening of the source over the course of the campaign was observed at all optical frequencies, culminating in a very bright maximum around Feb. 18, 2004. The WEBT campaign revealed microvariability with flux changes of $\sim 5\%$ on time scales as short as ~ 2 hr. The source was in a relatively bright state, with several bright flares on time scales of several days. The spectral energy distribution (SED) indicates a νF_ν peak in the optical regime. A weak trend of optical spectral hysteresis with a trend of spectral softening throughout both the rising and decaying phases, has been found. On longer time scales, there appears to be a weak indication of a positive hardness-intensity correlation for low optical fluxes, which does not persist at higher flux levels.

The 3 – 10 keV X-ray flux of 3C 66A during the core campaign was historically high and its spectrum very soft, indicating that the low-frequency component of the broadband SED extends beyond ~ 10 keV. No significant X-ray flux and/or spectral variability was detected. STACEE and Whipple observations provided upper flux limits at > 150 GeV and > 390 GeV, respectively.

The 22 and 43 GHz data from the 3 VLBA epochs made between September 2003 and January 2004 indicate a rather smooth jet with only very moderate internal structure. Evidence for superluminal motion ($8.5 \pm 5.6 h^{-1} c$) was found in only one out of 6 components, while the apparent velocities of all other components are consistent with 0. The radial radio brightness profile suggests a magnetic field decay $\propto r^{-1}$ and, thus, a predominantly perpendicular magnetic field orientation.

Subject headings: galaxies: active — BL Lacertae objects: individual (3C 66A) — gamma-rays: theory — radiation mechanisms: non-thermal

¹Astrophysical Institute, Department of Physics and Astronomy,
Clippinger 339, Ohio University, Athens, OH 45701, USA

²Istituto Nazionale di Astrofisica (INAF), Osservatorio
Astronomico di Torino,
Via Osservatorio 20, I-10025 Pino Torinese, Italy

³Barnard College, Columbia University, New York, NY
10027, USA

⁴Department of Physics and Astronomy, Rice Univer-
sity, MS 108,
6100 S. Main St., Houston, TX 77005-1892, USA

⁵Department of Physics, Purdue University, 525 North-
western Ave.,
West Lafayette, IN 47907-1396, USA

⁶Tuorla Observatory, University of Turku, 21500 Pi-
ikkiö, Finland

⁷Department of Astronomy, University of Michigan, 830
Dennison Building,
Ann Arbor, MI 48109-1090, USA

⁸Pulkovo Observatory, Pulkovskoye Shosse, 65, 196140,
St. Petersburg, Russia

⁹Department of Physics and Astronomy, Western Ken-
tucky University,
1 Big Red Way, Bowling Green, KY 42104, USA

¹⁰Boltwood Observatory, 1655 Stittsville Main St.,
Stittsville,
Ontario, Canada, K2S 1N6

¹¹Osservatorio di Armenzano, Assisi, Italy

¹²Osservatorio Astronomico, Università di Perugia, Via
B. Bonfigli,
I-06126 Perugia, Italy

¹³Agrupaciòn Astronómica de Sabadell, Sabadell 08200,
Spain

¹⁴Instituto de Astronomía, UNAM, Apdo. Postal 70-264,
04510 México DF, Mexico

¹⁵Center for Astrophysics, Guangzhou University,
Guangzhou 510400, China

¹⁶Osservatorio Astrofisico di Catania, Viale A. Doria 6,
I-95125 Catania, Italy

¹⁷Astronomical Institute, St. Petersburg State Univer-
sity,
Universitetsky pr. 28, Petrodvoretz, 198504 St. Petersburg,
Russia

¹⁸Isaac Newton Institute of Chile, St. Petersburg
Branch,
198504 St. Petersburg, Russia

¹⁹Ulugh Beg Astronomical Institute, Academy of Sci-
ences of Uzbekistan,
33 Astronomical Str., Tashkent 700052, Uzbekistan

²⁰Isaac Newton Institute of Chile, Uzbekistan Branch

²¹Abastumani Observatory, 383762 Abastumani, Geor-
gia

²²Department of Physics and Astronomy, Columbia Uni-
versity,
New York, NY 10027, USA

²³Michael Adrian Observatory, Astronomie-Stiftung Tre-

bur, Fichtenstrae 7,
D-65468 Trebur, Germany

²⁴Astronomical Institute, Osaka Kyoiku University,
Kashiwara-shi,
Osaka, 582-8582 Japan

²⁵Nyrölä Observatory, Jyväskylän Sirius ry, Kyllikinkatu
1,
40950 Jyväskylä, Finland

²⁶Physics Department, University of Crete, 710 03 Her-
aklion, Crete, Greece

²⁷IESL, Foundation for Research and Technology-Hellas,
711 10 Heraklion, Crete, Greece

²⁸Department of Physics and Astronomy, University of
Missouri-St. Louis,
8001 Natural Bridge Road, St. Louis, MO 63121, USA

²⁹Metsähovi Radio Observatory, Helsinki University of
Technology,
Metsähovintie 114, 02540 Kylmäla, Finland

³⁰Institute of Astronomy and Astrophysics, NOA, I.
Metaxa & Vas. Pavlou str.,
Palaia Penteli, Athens, Greece

³¹Korea Astronomy & Space Science Institute, 61-1
Whaam-Dong, Yuseong-Gu,
Daejeon 305-348, Korea

³²Shanghai Astronomical Observatory, Chinese Academy
of Sciences,
80 Nandan Road, Shanghai 200030, China

³³National Astronomical Observatories, Chinese
Academy of Sciences,
Beijing 100012, China

³⁴Physical Research Laboratory, Ahmedabad – 3800 009,
India

³⁵Nordic Optical Telescope, Apartado 474, E-38700
Santa Cruz de La Palma,
Santa Cruz de Tenerife, Spain

³⁶Astro Space Center, Profsoyuznaya St. 84/32, Moscow
117997, Russia

³⁷Harvard-Smithsonian Astrophysical Observatory, 60
Garden Street,
Cambridge, MA 02138, USA

³⁸Institute of Space and Astronautical Science, Japan
Aerospace Exploration Agency,
3-1-1 Yoshinodai, Sagami-hara, Kanagawa 229-8510, Japan

³⁹Landessternwarte Heidelberg-Königstuhl, Königstuhl,
D-69117 Heidelberg, Germany

⁴⁰Istituto Nazionale di Astrofisica (INAF), Osservatorio
Astronomico di Roma,
Via Frascati, Monteporzio Cantone, Roma, Italy

⁴¹Istituto Nazionale di Astrofisica (INAF), Osservatorio
Astronomico di Teramo,
Via Maggini, Teramo, Italy

⁴²National radio Astronomy Observatory, P. O. Box 2,
Green Bank, WV 24944, USA; Jansky Fellow

¹For questions regarding the availability of the data
from the WEBT campaign presented in this paper,
please contact the WEBT President Massimo Villata at

1. Introduction

BL Lac objects and flat-spectrum radio quasars (FSRQs) are active galactic nuclei (AGNs) commonly unified in the class of blazars. They exhibit some of the most violent high-energy phenomena observed in AGNs to date. They are characterized by non-thermal continuum spectra, a high degree of linear polarization in the optical, rapid variability at all wavelengths, radio jets with individual components often exhibiting apparent superluminal motion, and — at least episodically — a significant portion of the bolometric flux emitted in γ -rays. 46 blazars have been detected and identified with high confidence in high energy (> 100 MeV) gamma-rays by the EGRET instrument on board the *Compton Gamma-Ray Observatory* (Hartman et al. 1999; Mattox, Hartman, & Reimer 2001). The properties of BL Lac objects and blazar-type FSRQs are generally very similar, except that BL Lac objects usually show only weak emission or absorption lines (with equivalent width in the rest-frame of the host galaxy of < 5 Å), if any. In 3C 66A (= 0219+428 = NRAO 102 = 4C 42.07), a weak Mg II emission line has been detected by Miller, French, & Hawley (1978). This led to the determination of its redshift at $z = 0.444$, which was later confirmed by the detection of a weak Ly α line in the IUE spectrum of 3C 66A (Lanzetta, Turnshek, & Sandoval 1993). However, as recently pointed out by Bramel et al. (2005), these redshift determinations are actually still quite uncertain. In this paper, we do base our analysis on a redshift value of $z = 0.444$, but remind the reader that some results of the physical interpretation should be considered as tentative pending a more solid redshift determination.

In the framework of relativistic jet models, the low-frequency (radio – optical/UV) emission from blazars is interpreted as synchrotron emission from nonthermal electrons in a relativistic jet. The high-frequency (X-ray – γ -ray) emission could either be produced via Compton upscattering of low frequency radiation by the same electrons responsible for the synchrotron emission (leptonic jet models; for a recent review see, e.g., Böttcher 2002), or due to hadronic processes initiated by relativistic protons co-accelerated with the electrons (hadronic models, for a recent discussion see,

e.g., Mücke & Protheroe 2001; Mücke et al. 2003).

To date, 6 blazars have been detected at very high energies (> 300 GeV) with ground-based air Čerenkov detectors (Punch et al. 1992; Quinn et al. 1996; Catanese et al. 1998; Chadwick et al. 1999; Aharonian et al. 2002; Horan et al. 2002; Holder et al. 2003). All of these belong to the sub-class of high-frequency peaked BL Lac objects (HBLs). The field of extragalactic GeV – TeV astronomy is currently one of the most exciting research areas in astrophysics, as the steadily improving flux sensitivities of the new generation of air Čerenkov telescope arrays and their decreasing energy thresholds (for a recent review see, e.g., Weekes et al. 2002), provides a growing potential to extend their extragalactic-source list towards intermediate and even low-frequency peaked BL Lac objects (LBLs) with lower νF_ν peak frequencies in their broadband spectral energy distributions (SEDs). Detection of such objects at energies $\sim 40 - 100$ GeV might provide an opportunity to probe the intrinsic high-energy cutoff of their SEDs since at those energies, $\gamma\gamma$ absorption due to the intergalactic infrared background is still expected to be small (e.g., de Jager & Stecker 2002).

3C 66A has been suggested as a promising candidate for detection by the new generation of atmospheric Čerenkov telescope facilities like STACEE or VERITAS (e.g. Costamante & Ghisellini 2002). Neshpor et al. (1998, 2000) have actually reported multiple detections of the source with the GT-48 telescope of the Crimean Astrophysical Observatory, but those could not be confirmed by any other group so far (see, e.g. Horan et al. 2004).

3C 66A is classified as a low-frequency peaked BL Lac object (LBL), a class also commonly referred to as radio selected BL Lac objects. Its low-frequency spectral component typically peaks at IR – UV wavelengths, while the high-frequency component seems to peak in the multi-MeV – GeV energy range. Since its optical identification by Wills & Wills (1974), 3C 66A has been the target of many radio, IR, optical, X-ray, and γ -ray observations in the past, although it is not as regularly monitored at radio frequencies as many other blazars due to problems with source confusion with the nearby radio galaxy 3C 66B (6'.5 from 3C 66A), in particular at lower (4.8 and 8 GHz)

frequencies (Aller, Aller, & Hughes 1994; Takalo et al. 1996).

The long-term variability of 3C 66A at near-infrared (J, H, and K bands) and optical (U, B, V, R, I) wavelengths has recently been compiled and analyzed by Fan & Lin (1999) and Fan & Lin (2000), respectively. Variability at those wavelengths is typically characterized by variations over $\lesssim 1.5$ mag on time scales ranging from ~ 1 week to several years. A positive correlation between the B – R color (spectral hardness) and the R magnitude has been found by Vagnetti et al. (2003). An intensive monitoring effort by Takalo et al. (1996) revealed evidence for rapid microvariability, including a decline ~ 0.2 mag within ~ 6 hr. Microvariability had previously been detected in 3C 66A by Carini & Miller (1991) and De Diego et al. (1997), while other, similar efforts did not reveal such evidence (e.g. Miller & McGimsey 1978; Takalo et al. 1992; Xie et al. 1992). Lainela et al. (1999) also report on a 65-day periodicity of the source in its optically bright state, which has so far not been confirmed in any other analysis.

3C 66A is generally observed as a point source, with no indication of the host galaxy. The host galaxy of 3C 66A was marginally resolved by Wurtz, Stocke, & Yee (1996). They found $R_{\text{Gunn}} = 19.0^{\text{mag}}$ for the host galaxy; the Hubble type could not be determined.

In X-rays, the source has been previously detected by EXOSAT (Sambruna et al. 1994), EINSTEIN (Worrall & Wilkes 1990), ROSAT (Fosati et al. 1998), BeppoSAX (Perri et al. 2003), and *XMM-Newton* (Croston et al. 2003). It shows large-amplitude soft-X-ray variability among these various epochs of observation, with flux levels at 1 keV ranging from $\sim 0.4 \mu\text{Jy}$ to $\sim 5 \mu\text{Jy}$ and generally steep (energy index $\alpha > 1$) soft X-ray spectra below 1 keV. 3C 66A has also been detected in > 100 MeV γ -rays by *EGRET* on several occasions, with flux levels up to $F_{>100\text{MeV}} = (25.3 \pm 5.8) \times 10^{-8}$ photons $\text{cm}^{-2} \text{s}^{-1}$ (Hartman et al. 1999).

Superluminal motion of individual radio components of the jet has been detected by Jorstad et al. (2001). While the identification of radio knots across different observing epochs is not unique, Jorstad et al. (2001) favor an interpretation implying superluminal motions of up to $\beta_{\text{app}} \sim 19 h^{-1} \approx$

27. This would imply a lower limit on the bulk Lorentz factor of the radio emitting regions of $\Gamma \geq 27$. However, theoretical modeling of the non-simultaneous SED of 3C 66A (Ghisellini et al. 1998) suggests a bulk Lorentz factor of the emitting region close to the core — where the γ -ray emission is commonly believed to be produced — of $\Gamma \sim 14$, more typical of the values obtained for other blazars as well.

In spite of the considerable amount of observational effort spent on 3C 66A (see, e.g. Takalo et al. 1996, for an intensive optical monitoring campaign on this source), its multiwavelength SED and correlated broadband spectral variability behaviour are still surprisingly poorly understood, given its possible VHE γ -ray source candidacy. The object has never been studied in a dedicated multiwavelength campaign during the life time of *EGRET*. There have been few attempts of coordinated multiwavelength observations. For example, Worrall et al. (1984) present quasi-simultaneous radio, IR, optical, and UV observations of 3C 66A in 1983, but observations at different wavelength bands were still separated by up to ~ 2 weeks, and no simultaneous higher-energy data were available. This is clearly inadequate to seriously constrain realistic, physical emission models, given the established large-amplitude variability on similar time scales and the importance of the high-energy emission in the broadband SED of the source.

For this reason, we have organized an intensive multiwavelength campaign to observe 3C 66A from July 2003 through April 2004, focusing on a core campaign from Sept. – Dec. 2003. In §2, we describe the observations and data analysis and present light curves in the various frequency bands. Spectral variability patterns are discussed in §3, and the results of our search for inter-band cross-correlations and time lags are presented in §4. Simultaneous broadband spectral energy distributions (SEDs) of 3C 66A at various optical brightness levels are presented in §5. In §6 we use our results to derive estimates of physical parameters, independent of the details of any specific model. We summarize in §7. In a companion paper (Joshi & Böttcher, 2005, in preparation), we will use time-dependent leptonic models to fit the spectra and variability patterns found in this campaign, and make specific predictions concerning potentially observable X-ray spectral variabil-

ity patterns and γ -ray emission.

Throughout this paper, we refer to α as the energy spectral index, F_ν [Jy] $\propto \nu^{-\alpha}$. A cosmology with $\Omega_m = 0.3$, $\Omega_\Lambda = 0.7$, and $H_0 = 70 \text{ km s}^{-1} \text{ Mpc}^{-1}$ is used. In this cosmology, and using the redshift of $z = 0.444$, the luminosity distance of 3C 66A is $d_L = 2.46 \text{ Gpc}$.

2. Observations, data reduction, and light curves

3C 66A was observed in a coordinated multiwavelength campaign at radio, near-IR, optical (by the WEBT-ENIGMA collaboration), X-ray, and VHE γ -ray energies during a core campaign period of September 2003 – December 2003. The object is being continuously monitored at radio and optical wavelength by several ongoing projects, and we present data in those wavelengths regimes starting in July 2003. During the core campaign, we found that the source was gradually brightening, indicating increasing activity throughout the campaign period. For this reason, the WEBT campaign was extended, and we continued to achieve good time coverage until early March 2004, and individual observatories still contributed data through April 2004. The overall timeline of the campaign, along with the measured long-term light curves at radio, infrared, optical, and X-ray frequencies is illustrated in Fig. 1. Table 1 lists all participating observatories which contributed data to this campaign. In this section, we will describe the individual observations in the various frequency ranges and outline the data reduction and analysis.

2.1. Radio observations

At radio frequencies, the object was monitored using the University of Michigan Radio Astronomy Observatory (UMRAO) 26 m telescope, at 4.8, 8, and 14.5 GHz, the 14 m Metsähovi Radio Telescope of the Helsinki University of Technology, at 22 and 37 GHz, and the 576-m ring telescope (RATAN-600) of the Russian Academy of Sciences, at 2.3, 3.9, 7.7, 11, and 22 GHz.

At the UMRAO, the source was monitored in the course of the on-going long-term blazar monitoring program. The data were analyzed following the standard procedure described in Aller et al. (1985). As mentioned above, the sampling at the

lower frequencies (4.5 and 8 GHz) was rather poor (about once every 1 – 2 weeks) and some individual errors were rather large due to source confusion problems with 3C 66B. At 14.5 GHz, a slightly better sampling of $\sim 1 - 2$ observations per week, at least until the end of 2003, was achieved with relative flux errors of typically a few percent. The resulting 14.5 GHz light curve is included in Fig. 1. It seems to indicate generally moderate variability ($\Delta F/F \lesssim 25 \%$) on time scales of $\gtrsim 1$ week, though a discrete auto-correlation analysis (Edelson & Krolik 1988) does not reveal any significant structure, primarily due to the insufficient sampling.

At 22 and 37 GHz, 3C 66A has been monitored using the 14 m radio telescope of the Metsähovi Radio Observatory of the Helsinki University of Technology. The data have been reduced with the standard procedure described in Teräsranta et al. (1998). The 22 and 37 GHz light curves reveal moderate-amplitude ($\Delta F/F \lesssim 30 \%$), erratic variability which is clearly under-sampled by the available data. The discrete auto-correlation functions indicate a time scale of a few days for this short-term variability.

We point out that the observed erratic variability may, at least in part, be a consequence of interstellar scintillation. At the Galactic coordinates of the source, the transition frequency, where the interstellar scattering strength (a measure of the phase change induced by interstellar scattering) becomes unity, is $\sim 7 \text{ GHz}$ (Walker 1998). At higher frequencies, as considered here, scattering will occur in the weak scattering regime, with only small phase changes through interstellar scattering. In this regime, we find the fractional rms variability amplitude for a point source due to interstellar scintillation as 0.36 and 0.09 at a frequency of 14.5 and 37 GHz, respectively, and the respective variability time scales due to interstellar scintillation are 1.4 and 0.9 hours. Consequently, in particular at lower frequencies ($\lesssim 20 \text{ GHz}$), a substantial fraction of the observed variability may well be due to interstellar scintillation.

The RATAN-600 has monitored 3C 66A, performing 17 observations from mid-1997 through Oct. 2003. The last two of these observations (Oct. 11 and 14) coincided with our core campaign, and provided additional frequency coverage at 2.3, 3.9, 7.7, 11, and 22 GHz. Those data

TABLE 1
LIST OF OBSERVATORIES THAT CONTRIBUTED DATA TO THIS CAMPAIGN

Observatory	Specifications	frequency / filters / energy range	N_{obs}
Radio Observatories			
UMRAO, Michigan, USA	26 m	4.8, 8, 14.5 GHz	46
Metsähovi, Finland	14 m	22, 37 GHz	103
RATAN-600, Russia	576m (ring)	2.3, 3.9, 7.7, 11, 22 GHz	17
VLBA	10x25 m	2.3, 5, 8.4, 22, 43, 86 GHz	9
Infrared Observatories			
Campo Imperatore, Italy	1.1 m	J, H, K	171
Mt. Abu, India (MIRO)	1.2 m (NICMOS-3)	J, H, K'	79
Roque (NOT), Canary Islands	2.56 m	J, H, K	15
Optical Observatories			
Abastumani, Georgia (FSU)	70 cm	R	210
Armenzano, Italy	40 cm	B, V, R, I	315
Bell Obs., Kentucky, USA	60 cm	R	12
Boltwood, Canada	40 cm	B, V, R, I	402
Catania, Italy	91 cm	U, B, V	835
Crimean Astr. Obs., Ukraine	70 cm ST-7	B, V, R, I	85
Heidelberg, Germany	70 cm	B, R, I	8
Kitt Peak (MDM), Arizona, USA	130 cm	B, V, R, I	147
Michael Adrian Obs., Germany	120 cm	R	30
Mt. Lemmon, Korea	100 cm	B, V, R, I	399
Mt. Maidanak, Uzbekistan	150 cm AZT-22	B, R	1208
Nyrölä, Finland	40 cm SCT	R	159
Osaka Kyoiku, Japan	51 cm	R	1167
Perugia, Italy	40 cm	V, R, I	140
Roque (KVA), Canary Islands	35 cm	B, V, R	653
Roque (NOT), Canary Islands	256 cm	U, B, V, R, I	52
Sabadell, Spain	50 cm	B, R	4
San Pedro Martír, Mexico	150 cm	B, V, R, I	185
Shanghai, China	156 cm	V, R	36
Skinakas, Crete	130 cm	B, V, R, I	156
Sobaeksan, Korea	61 cm	B, V, R, I	133
St. Louis, Missouri, USA	35 cm	B, R	16
Torino, Italy	105 cm REOSC	B, V, R, I	227
Tuorla, Finland	103 cm	B, V, R	1032
X-Ray Observatory			
RXTE	PCA	3 – 25 keV	26
γ-Ray Observatories			
STACEE	Solar-Tower Cerenkov Array	> 100 GeV	85
VERITAS	Whipple 10 m	> 390 GeV	31

were analyzed as described in detail in Kovalev et al. (1999), and the time average of the resulting fluxes from the two observations in Oct. 2003 are included in the spectral energy distribution shown in fig. 15.

A total of 9 observing epochs using the VLBA² have been approved to accompany our multiwavelength campaign on 3C 66A. In this paper, we describe details of the data analysis and results of the first (2003.78; VLBA observing code BS133A), the second (2003.83; BS133B), and the fourth (2004.08; BS133E) epoch, concentrating on the results at 22 and 43 GHz. The third epoch (2003.96) suffered from radio frequency interference, and its reduction is in progress. Results of the complete set of all 9 VLBA observing epochs, including all 6 frequencies (2.3, 5, 8.4, 22, 43, and 86 GHz) together with polarization data, will be presented in a separate paper (Savolainen et al., 2005, in preparation).

The data were correlated on the VLBA correlator and were postprocessed with the NRAO Astronomical Image Processing System, AIPS (Greisen 1988), and the Caltech DIFMAP package (Shepherd 1997). Standard methods for VLBI data reduction and imaging were used. *A priori* amplitude calibration was performed using measured system temperatures and gain curves in the AIPS task APCAL. At this point, a correction for atmospheric opacity was also applied. After removal of the parallactic angle phase, single-band delay and phase offsets were calculated manually by fringe-fitting a short scan of data of a bright calibrator source (0420-014). We did manual phase calibration instead of using pulse-cal tones, because there were unexpected jumps in the phases of the pulse-cal during the observations. Global fringe-fitting was performed with the AIPS task FRING using Los Alamos (LA) as a reference antenna. The AIPS procedure CRSFRING was used to remove the delay difference between right- and left-hand systems (this is needed for polarization calibration). A bandpass correction was determined and applied before averaging across the channels, after which the data were imported into DIFMAP.

²The VLBA is a facility of the National Radio Astronomy Observatory (NRAO). The NRAO is a facility of the National Science Foundation, operated under cooperative agreement by Associated Universities, Inc.

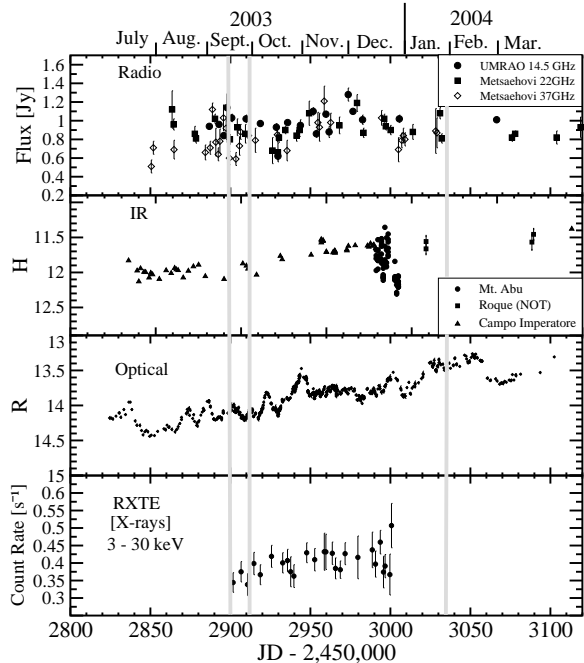


Fig. 1.— Timeline of the broadband campaign on 3C 66A in 2003/2004. The grey vertical lines indicate the epochs of the VLBA observations.

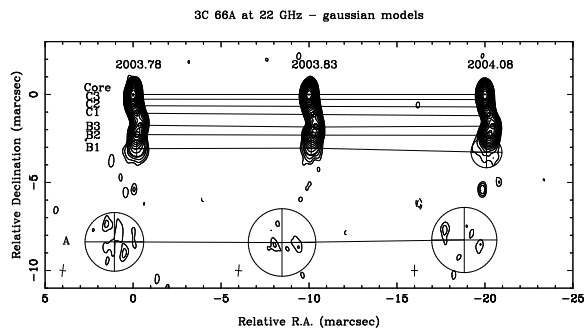


Fig. 2.— 22-GHz VLBA maps of 3C 66A during the three epochs in 2003/2004 contemporaneous with our campaign. Overlaid are the fit results from decomposing the structure into a sum of Gaussian components.

In DIFMAP, the data were first phase self-calibrated using a point source model, and then averaged in time. We performed data editing in a station-based manner, and ran several iterations of CLEAN and phase self-calibration in Stokes I. After a reasonable fit to the closure phases was obtained, we also performed amplitude self-calibration, first with a solution interval corresponding to the whole observation length. The solution interval was then gradually shortened as the model improved by further CLEANing. Final images were produced using the Perl library FIT-Splot³. For final images, normal weighting of the uv-data was used in order to reveal the extended, low surface brightness emission.

We have checked the amplitude calibration by comparing the extrapolated zero baseline flux density of the compact source 0420-014 to the single-dish flux measurements at Metsähovi. The fluxes are comparable: at 22 GHz the VLBI flux is on average 5 % lower than the single-dish flux, and the 43 GHz flux is on average 8 % lower than the nearly simultaneous single-dish measurements at 37 GHz. The small amount of missing flux is probably due to some extended emission resolved out in the high frequency VLBI images. The integrated VLBI flux of 3C 66A is about 30 % smaller than the corresponding single-dish value both at 22 GHz and at 43 GHz, but since the source has notable kpc-scale structure evident in the VLA images (Price et al. 1993; Taylor et al. 1996), it is most likely that the missing flux comes from this kpc-scale jet which is resolved out in our VLBI images. Thus, we conclude that the accuracy of the amplitude calibration is better than 10 % at both frequencies.

In order to estimate the parameters of the emission regions in the jet, we did model fitting to the self-calibrated visibilities in DIFMAP. The data were fitted with circular Gaussian model components and we sought to obtain the best possible fit to the visibilities and to the closure phases. Several starting points were tried in order to avoid a local minimum fit. The results of this fitting procedure are included in Figs. 2 and 3. In all the model-fits, the core of the VLBI jet is the northernmost and also the brightest component. Beyond the core, we have divided the jet into three

regions named A, B and C. Closest to the core is the region C, which consists of three components with decreasing surface brightness as a function of the distance from the core. The region B, also made of three components, shows a clear bending of the jet together with re-brightening. The observed increase in the flux at this point could plausibly be due to increased Doppler boosting caused by the bending of the jet towards our line of sight. The region A shows weak extended emission at 8 mas from the core at 22 GHz. This emission is more pronounced at lower frequencies.

Fig. 4 shows the separation of the model components from the core, at each epoch. The components A - C are weak compared to the core (see Table 3), which renders the estimation of errors of the model parameters using programs like Difwrap (Lovell 2000) problematic. Thus, in Fig. 4, we have assumed the following uncertainties in the component position accuracy: 1) for bright features with $SNR > 50$, the positions are accurate to 20 % of the projection of the elliptical beam FWHM onto a line joining the center of the core to the center of the components; 2) for weaker components with $SNR < 50$, uncertainties are 50 % of the beam size or 50 % of the size of the knot — whichever is larger. These estimates are based on the experience with other sources (Savolainen et al. 2005, in preparation; Wiik et al. 2005, in preparation), and they follow the results by Jorstad et al. (2005), where uncertainties of model-fit parameters for a large number of observations are estimated. Positional errors of similar size are also reported by Homan et al. (2001), who have estimated the uncertainties from the variance of the component position about the best-fit polynomial.

There is a ~ 0.1 mas shift of the components C1 - C3 between the two frequencies, with the 22 GHz model components appearing further downstream. This cannot be explained by an opacity effect, since in that case the components would have shifted in the opposite direction: at higher frequency we would expect to see emission from the region closer to the apex of the jet than at lower frequency, if the opacity effect is significant. This obviously is not the case in Fig. 4, and moreover, for the components B2 and B3 the positions at 22 and 43 GHz are coincident. However, there is a simple explanation for the observed shift, if

³<http://personal.denison.edu/~homand/>

TABLE 2

CORE BRIGHTNESS TEMPERATURES AND CORRESPONDING LOWER LIMITS, CALCULATED FROM THE MEASURED 43 GHz VLBA FLUXES AND COMPONENT SIZES

Epoch	T_b^{core} [K]	$T_{b,\text{min}}^{\text{core}}$ [K]
2003.78	2.7×10^{11}	1.1×10^{11}
2003.83	2.0×10^{11}	1.0×10^{11}
2004.08	6.6×10^{11}	1.4×10^{11}

TABLE 3

VLBA COMPONENT FLUXES, CORE DISTANCES (RAD.), COMPONENT POSITION ANGLES (PA), AND CIRCULAR COMPONENT DIAMETERS (SIZE)

Epoch	Freq. [GHz]	Comp. ID	Flux [mJy]	Rad. [mas]	PA [deg]	Size [mas]
2003.78	22 GHz	Core	387	0.0	0.0	0.047
		C3	61	0.295	-172.9	0.136
		C2	36	0.658	-168.2	0.164
		C1	19	1.096	-167.9	0.309
		B3	21	1.803	-166.1	0.278
		B2	40	2.287	-174.6	0.331
		B1	19	3.086	-176.2	0.970
	A	37	8.439	172.8	3.333	
	43 GHz	Core	355	0.0	0.0	0.029
		C3	63	0.183	-174.0	0.089
		C2	43	0.534	-171.1	0.218
		C1	24	0.940	-165.4	0.304
		B3	18	1.849	-167.3	0.284
		B2	30	2.279	-173.8	0.329
B1		9	2.821	-173.8	0.349	
2003.83	22 GHz	Core	375	0.0	0.0	0.032
		C3	59	0.282	-172.4	0.118
		C2	38	0.685	-170.2	0.193
		C1	18	1.167	-167.3	0.298
		B3	23	1.892	-167.7	0.274
		B2	39	2.320	-174.8	0.358
		B1	13	3.051	-177.6	0.836
	A	41	8.546	169.7	3.836	
	43 GHz	Core	369	0.0	0.0	0.034
		C3	76	0.187	-176.3	0.116
		C2	34	0.584	-172.1	0.210
		C1	26	1.050	-166.0	0.383
		B3	26	1.947	-168.6	0.385
		B2	20	2.328	-175.0	0.213
B1		16	2.829	-174.1	0.795	
2004.08	22 GHz	Core	363	0.0	0.0	0.046
		C3	64	0.289	-172.4	0.132
		C2	32	0.712	-172.0	0.235
		C1	12	1.241	-167.2	0.311
		B3	22	1.860	-165.7	0.296
		B2	45	2.333	-174.2	0.386
		B1	18	3.285	-178.5	1.754
	A	38	8.348	171.9	3.702	
	43 GHz	Core	372	0.0	0.0	0.019
		C3	59	0.207	-171.2	0.078
		C2	30	0.568	-171.6	0.207
		C1	13	1.109	-166.2	0.252
		B3	15	1.816	-166.3	0.320
		B2	40	2.289	-173.7	0.411
X1		4	3.375	-171.8	0.417	

the brightness profile along the jet in region C is smooth. Namely, the flux in the outer part of the region C decreases more steeply at 43 GHz than at 22 GHz (see Figs. 2 and 3). As the region C is modelled by the same number of components at both frequencies, the model-fit procedure shifts the 22 GHz components downstream relative to 43 GHz components in order to represent the power-law.

Fig. 4 shows that, except for one component, all the components revealed by the analysis of the three epochs considered here are consistent with zero proper motion. Although a monitoring effort over a longer time scale will be necessary to settle this issue, our analysis shows slower component motion than what is presented by Jorstad et al. (2001), where fast superluminal motions of several components, with speeds ranging from $9 h^{-1} c$ to $19 h^{-1} c$ were found. Note, however, that the data used by Jorstad et al. (2001) covered a much longer time frame and refers to different components and a rather different state of activity of 3C 66A. Moreover, there are also similarities between the data sets: Jorstad et al. (2001) reported a stationary component (their component "C") at distance of ~ 0.5 mas from the core, which could correspond to our component C2. New 7 mm VLBA monitoring data presented in a recent paper by Jorstad et al. (2005) suggest that there are two kinds of components in 3C 66A: fast and very weak components with apparent speeds $> 20 c$, and stronger components with moderate velocities of $1.5 - 5 c$. The components C1 – C3 in our analysis could be qualitatively similar to the latter. More solid conclusions concerning the question of superluminal motions of individual components might be possible after the final analysis of all 9 epochs of the entire VLBA monitoring program of 3C66A proposed in connection with this campaign (Savolainen et al., 2005, in preparation). Based on the analysis of the three epochs contemporaneous with the other observations of this campaign, one component, C1, shows superluminal motion of $(8.5 \pm 5.6) h^{-1} c = (12.1 \pm 8.0) c$ for $h = 0.7$.

The essentially zero proper motion of most of the components together with the observed trend of the brightness temperature vs. distance along the jet (see §6.2) suggest that in the case of 3C 66A the VLBA model-fit components might not correspond to actual 'knots' in the jet, but a rather

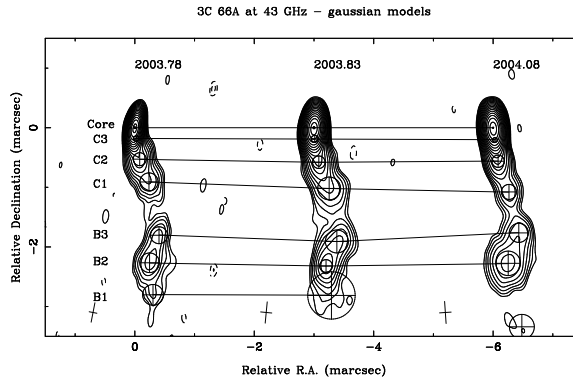


Fig. 3.— 43-GHz VLBA maps of 3C 66A during the three epochs in 2003/2004 contemporaneous with our campaign. Overlaid are the fit results from decomposing the structure into a sum of Gaussian components.

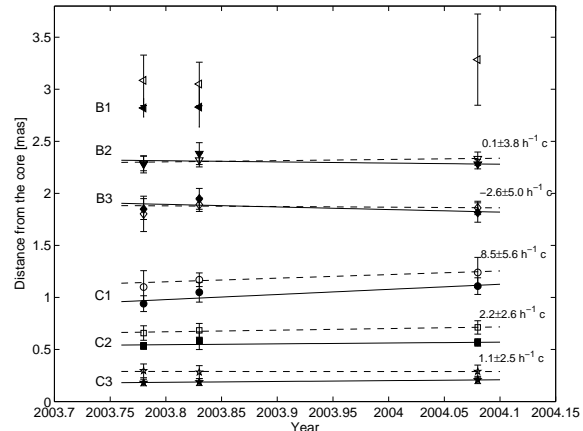


Fig. 4.— Separation from the core of the Gaussian fit components shown in Figs. 2 and 3, as a function of time. Filled symbols refer to 22 GHz, open symbols to 43 GHz. The solid (dashed) lines show linear least-squares fits to the positions of 22 GHz (43 GHz) components. The velocity results are the average of the results from the two frequencies. All components except C1 are consistent with being stationary.

smooth flow with simple brightness profile (such as a power law) might better describe the jet during this campaign — at least in region C. More detailed parameter estimates will be extracted from these results in §6.2.

2.2. Infrared observations

In the context of the extensive WEBT campaign (see §2.3), 3C 66A was also observed at near-infrared wavelengths in the J, H, and K/K' bands at three observatories: The Campo Imperatore 1.1-m telescope of the Infrared Observatory of the Astronomical Observatory of Rome, Italy, the 1.2-m telescope (using the NICMOS-3 HgCdTe IR array with 256×256 pixels, with each pixel corresponding to $0.96''$ on the sky) at the Mt. Abu Infrared Observatory (MIRO) at Mt. Abu, India, and at the 2.56-m Nordic Optical Telescope (NOT) on Roque de los Muchachos on the Canary Island of La Palma. The primary data were analyzed using the same standard technique as the optical data (see §2.3), including flat-field subtraction, extraction of instrumental magnitudes, calibration against comparison stars to obtain standard magnitudes, and de-reddening. The sampling was generally not dense enough to allow an improvement of the data quality by re-binning. Unfortunately, the three observatories did not perform any observations on the same day, so that the cross-calibration between different instruments is problematic. We have therefore opted not to correct for possible systematic offsets beyond the calibration to standard magnitudes of well-calibrated comparison stars (see §2.3).

The resulting H-band light curve is included in Fig. 1, and a comparison of all three IR band light curves (J, H, K/K') is shown in Fig. 5. Generally, we find moderate variability of $\Delta(J, H, K/K') \lesssim 0.2$ within \sim a few days. The various infrared bands trace each other very well, and there does not appear to be any significant time lags between the different bands. It is obvious that there are issues with the cross calibration between the three observatories. In particular, the Mt. Abu observations (using the J, H, and K' filters) in mid-December of 2003 indicate a significant drop of the average level of near-infrared flux. While there appears to be a similar flux drop around the same time in the radio light curves, the much more densely sampled optical light curves do not indi-

cate a similar feature. However, it is obvious that the near-IR data around this time exhibit an unusually large scatter (by ~ 0.5 mag on sub-hour time scales), they may be affected by calibration uncertainties. We note that rebinning of the IR data in time bins of up to 30 minutes did not improve the quality of the data because of the extreme nature of the apparent flux fluctuations. We also point out that the use of the K' filter at Mt. Abu vs. the K filter at the other two IR observatories, could only explain offsets of less than the individual measurement errors, so this effect was neglected in our analysis.

2.3. Optical observations

In the optical component of the extensive WEBT campaign, 24 observatories in 15 countries contributed 7611 individual photometric data points. The observing strategy and data analysis followed to a large extent the standard procedure described previously for a similar campaign on BL Lacertae in 2000 (Villata et al. 2002). For more information about WEBT campaigns see also: Villata et al. (2000, 2002, 2004a,b); Raiteri et al. (2001, 2005)

It had been suggested that, optimally, observers perform photometric observations alternately in the B and R bands, and include complete (U)BVRI sequences at the beginning and the end of each observing run. Exposure times should be chosen to obtain an optimal compromise between high precision (instrumental errors less than ~ 0.03 mag for small telescopes and ~ 0.01 mag for larger ones) and high time resolution. If this precision requirement leads to gaps of 15 – 20 minutes in each light curve, we suggested to carry out observations in the R band only. Observers were asked to perform bias (dark) corrections as well as flat-fielding on their frames, and obtain instrumental magnitudes, applying either aperture photometry (using IRAF or CCDPHOT) or Gaussian fitting for the source 3C 66A and the comparison stars no. 13, 14, 21, and 23 in the tables of González-Pérez et al. (2001), where high-precision standard magnitudes for these stars have been published. This calibration has then been used to convert instrumental to standard photometric magnitudes for each data set. In the next step, unreliable data points (with large error bars at times when higher-quality data points were available)

were discarded. Our data did not provide evidence for significant variability on sub-hour time scales. Consequently, error bars on individual data sets could be further reduced by re-binning on time scales of typically 15 – 20 min.

Finally, there may be systematic offsets between different instruments and telescopes. Whenever our data sets contained sufficient independent measurements to clearly identify such offsets, individual data sets were corrected by applying appropriate correction factors. In the case of BL Lacertae and similar sources (e.g., Villata et al. 2002), such corrections need to be done on a night-by-night basis since changes in the seeing conditions affect the point spread function and thus the precise amount of the host galaxy contamination. However, in the absence of a significant host galaxy contribution, these systematic effects should be purely instrumental in nature and should thus not depend on daily seeing conditions. Thus, we opted to introduce only global correction factors for entire single-instrument data sets on 3C 66A. This provided satisfactory results without obvious residual inter-instrumental inconsistencies. The resulting offsets are listed in Tab. 4.

In order to provide information on the intrinsic broadband spectral shape (and, in particular, a reliable extraction of B - R color indices), the data were de-reddened using the Galactic Extinction coefficients of Schlegel et al. (1998), based on $A_B = 0.363$ mag and $E(B - V) = 0.084$ mag⁴. As mentioned in the introduction, the R magnitude of the host galaxy of 3C 66A is ~ 19 mag, so its contribution is negligible, and no host-galaxy correction was applied.

2.3.1. Light curves

As a consequence of the observing strategy described above, the R- and B-band light curves are the most densely sampled ones, resulting in several well-sampled light curve segments over $\sim 5 - 10$ days each, with no major interruptions, except for a gap of a few hours due to the lack of coverage when 3C 66A would have been optimally observable from locations in the Pacific Ocean. The R-band light curve over the entire duration of the campaign is included in Fig. 1 and com-

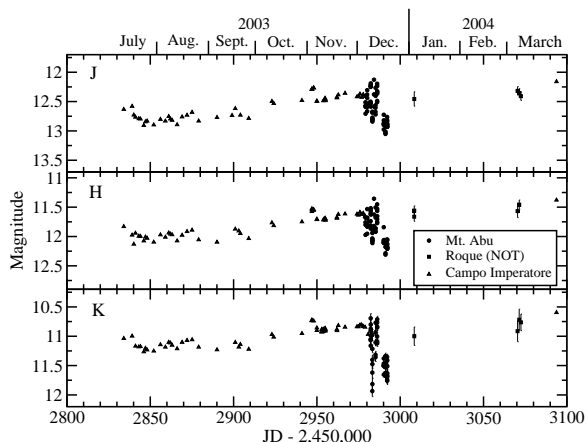


Fig. 5.— Light curves in the near-infrared J, H, and K bands over the entire duration of the campaign.

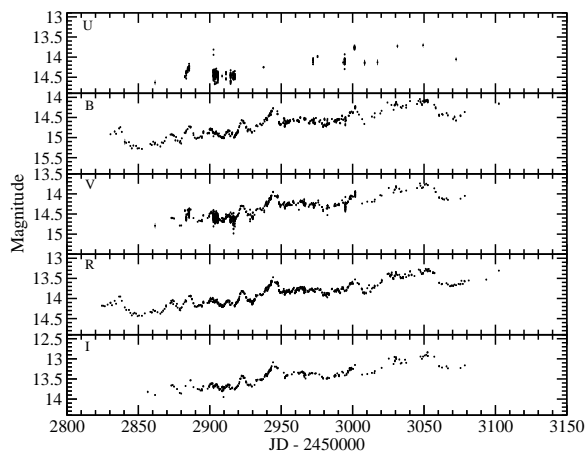


Fig. 6.— Light curves in the optical U, B, V, R, and I bands over the entire duration of the campaign.

⁴<http://nedwww.ipac.caltech.edu/>

TABLE 4
INTER-INSTRUMENTAL CORRECTION OFFSETS FOR OPTICAL DATA

Observatory	B	V	R	I
Armenzano	+0.02	-	+0.02	-
Bell	-	-	-	-
Boltwood	-0.02	-	-	-
Catania	-	-	-	-
Crimea	-	+0.03	-	-
Heidelberg	-	-	-	-
MDM	-	-	-	-
Michael Adrian	-	-	-	-
Mt. Lemmon	-	-	-	-
Mt. Maidanak	+0.01	-	-	-
Nyrola	-	-	-0.03	-
Osaka	-	-	-	-
Perugia	-	+0.08	+0.05	+0.04
Roque(NOT)	-	-	-	-
Sabadell	-	-	-	-
San Pedro Martir	+0.08	-	+0.07	-
Shanghai	-	-	-0.03	-
Skinakas	-0.01	-0.04	-0.04	-0.05
Sobaeksan	-	-	-	-
St. Louis	-0.06	-	-	-
Torino	-0.09	-	-	-0.03
Tuorla	-	+0.02	-0.02	-

pared to the light curves at all other optical bands in Fig. 6. These figures illustrate that the object underwent a gradual brightening throughout the period July 2003 – February 2004, reaching a maximum at $R \approx 13.4$ on Feb. 18, 2004, followed by a sharp decline by $\Delta R \sim 0.4$ mag within ~ 15 days. On top of this overall brightening trend, several major outbursts by $\Delta R \sim 0.3 - 0.5$ mag on time scales of ~ 10 days occurred. The two most dramatic ones of these outbursts peaked on July 18, 2003, and Nov. 1, 2003. Details of the Nov. 1 outburst are displayed in Figs. 7 – 9, respectively. We find evidence for intraday microvariability of $\Delta R \sim 0.05$ mag on time scales down to ~ 2 hr. One example for such evidence is illustrated in Fig. 10 which shows the intranight data from the Torino Observatory for JD 2,452,955 (= Nov. 11, 2003). The figure presents the instrumental magnitudes of 3C 66A, comparison star A, and the difference of both. While the difference seems to be affected by seeing effects at the beginning and end of the observation (rising and falling in tandem with the instrumental magnitudes), there is evidence for intraday variability around \sim JD 2,452,955.5, where there were only very minor changes in the atmospheric opacity.

Visual inspection of individual major outbursts suggests periods of more rapid decline than rise.

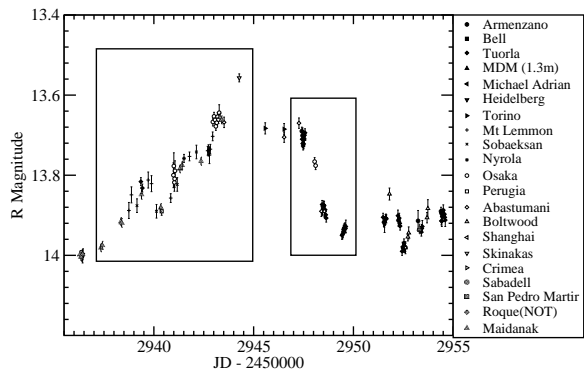


Fig. 7.— Details of the R-band light curve during the major outburst around Nov. 1, 2003. The boxes indicate the light curve segments shown in more detail in Figs. 8 – 9.

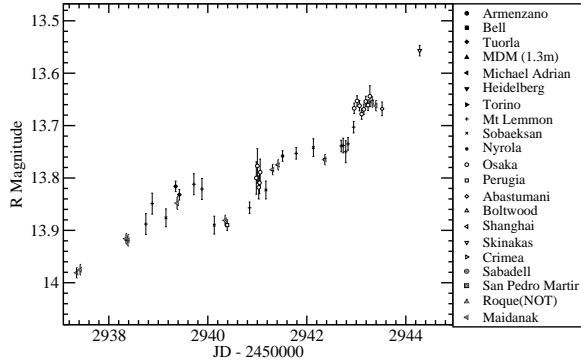


Fig. 8.— Details of the R-band light curve during the rising phase of the major outburst around Nov. 1, 2003.

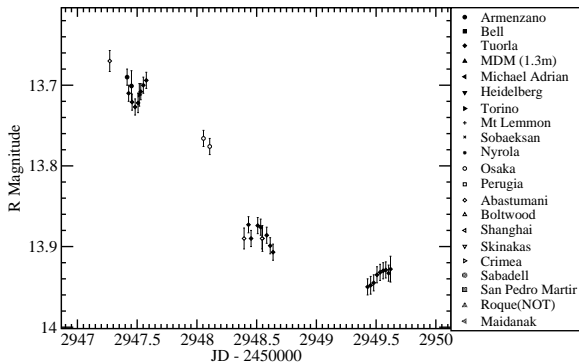


Fig. 9.— Details of the R-band light curve during the decaying phase of the major outburst around Nov. 1, 2003.

2.3.2. Periodicity analysis

For several blazars, including 3C 66A, periodicities on various time scales, from several tens of days, to several years, have been claimed (see, e.g. Rieger 2004, and references therein for a more complete discussion). In order to search for a possible periodicity in the optical R-band light curve from our WEBT campaign, we have performed a Fourier analysis of the R-band light curve after interpolation of the light curve over the (short) gaps in the available data. Such an analysis becomes unreliable for periods of more than $\sim 1/10$ of the length of the data segment. Consequently, our data can be used for a meaningful analysis on time scales of $\tau \lesssim 30 - 50$ d. No evidence for a periodicity in this range has been found. However, we note a sequence of large outbursts on July 18 (MJD 52838), Sept. 5 (MJD 52887), Nov. 1 (MJD 52944), Dec. 28 (MJD 53001), 2003, and Feb. 18, 2004 (MJD 53053), which are separated by intervals of 49, 57, 57, and 52 days, respectively. These intervals appear remarkably regular, and only slightly shorter than the 65-day period claimed by Lainela et al. (1999). The duration of our monitoring campaign is too short to do a meaningful analysis of the statistical significance of this quasi-periodicity. This question will be revisited in future work, on the basis of a larger data sample, including archival optical data.

2.4. X-ray observations

3C 66A was observed by the Rossi X-Ray Timing Explorer (*RXTE*) 26 times between September 19 and December 27, 2003, for a total observation time of approximately 200 ks. Analysis of the *RXTE* PCA data was carried out using faint-source procedures as described in the *RXTE* Cookbook. Standard selection criteria were used to remove disruptions from the South Atlantic Anomaly, bright Earth, instrument mispointing, and electron contamination. For the entire data set, only PCUs 0 and 2 were activated, but data from PCU 0 was discarded due to its missing propane veto. There is also a persistent problem in the background model of the PCA around the 4.78 keV Xenon L-edge, which causes a small anomaly in count rates near this energy. For faint sources like 3C 66A, this anomaly can be significant, so photons in the three energy bins surrounding this

energy were discarded.

Photons from 3 – 10 keV were extracted from the data using only the top layer of PCU2. Extracting higher-energy photons proved unreliable, as the source flux was close to the PCA source-confusion limit. A spectrum was compiled using data from all 26 source observations. The spectrum was fit to a simple power-law, which resulted in an energy spectral index of $\alpha = 1.47 \pm 0.56$ and a flux $\Phi_{1\text{ keV}} = (4.06 \pm 0.49) \times 10^{-3}$ photons $\text{cm}^{-2} \text{ s}^{-1} \text{ keV}^{-1}$, with $\chi^2/n = 13.6/14$. Galactic absorption was not included in the fit model, as the lack of data below 3 keV precludes a useful constraint on N_H . A plot of the spectrum and fit is shown in Figure 11.

The PCA is a non-imaging instrument with a FWHM response of 1° , so there is the potential that the signal found here is a sum over multiple sources. Most notably, the FR-1 galaxy 3C 66B lies only $6'$ from 3C 66A and is a known X-ray emitter. Though indistinguishable from 3C 66A with the PCA, its typical flux is at a level of $\sim 2\%$ of the measured PCA flux of 3C 66A (Croston et al. 2003), and is thus not a significant contributor. In the 3EG catalog, there is also confusion of 3C 66A with a nearby pulsar, PSR J0218+4232. At a source separation of $58'$, the PCA response for the pulsar is low for 3C 66A pointed observations, and thus it does not make a significant contribution.

The 3 – 10 keV photons were binned into 24-hour periods to render a light curve, which is included in Fig. 1. No significant flux variations or transient events were seen. To check for spectral variations, the data set was divided into four roughly equal sub-periods, and power-law spectra fitted to each sub-period. Fits to all four sub-periods were consistent with the spectral parameters obtained from the entire data set, and all sub-periods were consistent with each other. From this we conclude that there were no variations of either flux or spectral shape in the X-ray band during the observing period within the detection capabilities of *RXTE*.

2.5. Gamma-ray observations

At VHE γ -rays, 3C 66A was observed contemporaneously with our broadband campaign by the Solar Tower Air Čerenkov Effect Experiment

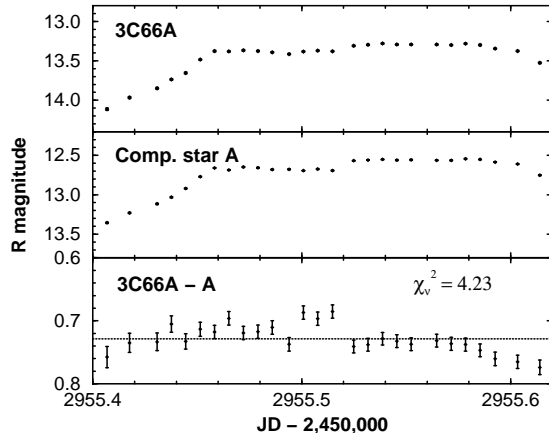


Fig. 10.— Instrumental magnitudes of 3C 66A (top panel) and comparison star A (central panel) of the University of Torino data of JD 2,452,955 (= Nov. 11, 2003). The difference (bottom panel) shows clear evidence for intranight variability during the central portion of this observation (\sim JD 2,452,955.4 – \sim JD 2,452,955.5).

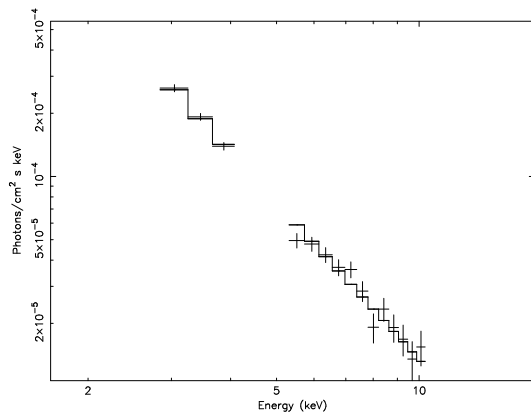


Fig. 11.— Average RXTE spectrum (3 – 10 keV) and power-law fit for all observations of 3C 66A taken as part of the multiwavelength campaign. See text for best-fit parameters.

(STACEE) and by the 10-m Whipple Telescope of the Very Energetic Radiation Imaging Telescope Array System (VERITAS) collaboration.

STACEE took a total of 85 28-minute on-off pairs of data, totalling 33.7 hours of live time on-source. After data-quality cuts and padding, a total of 16.3 hours of on-source live time remained. A net on-source excess of 1134 events attributed to photons of energy $E > 100$ GeV was seen against a background of 231,742 events. The details of the STACEE data analysis are published in a separate paper (Bramel et al. 2005).

The source excess quoted above corresponds to a significance of 2.2σ , which is insufficient to claim a detection, but can be used to establish firm upper flux limits. For various assumptions of an underlying intrinsic source power-law spectrum, those upper limits are listed in Table 5. The data were also binned in 24-hr segments. This revealed no significant excess on any given day, and thus no evidence for a statistically significant transient event during the campaign period.

The VERITAS collaboration observed 3C 66A during the period Sept. 27, 2003 – Jan. 13, 2004, obtaining a total of 31 on-off pairs with typically ~ 27.6 min. of on-source live time per pair. The data were analyzed following the standard Whipple data analysis procedure (see, e.g. Falcone et al. 2004). The log of the individual observations and 99.9 % confidence upper limits, assuming an underlying Crab-like source spectrum with an underlying energy index of 2.49 (Hillas et al. 1998), are listed in Table 6. Combining all measurements results in a 99.9 % confidence upper limit of 0.91×10^{-11} ergs cm^{-2} s^{-1} .

3. Spectral variability

In this section, we will describe spectral variability phenomena, i.e. the variability of spectral (and color) indices and their correlations with monochromatic source fluxes. As already mentioned in the previous section, no evidence for spectral variability in the X-ray regime was found. Consequently, we will concentrate here on the optical spectral variability as indicated by a change of the optical color. In particular, our observing strategy was optimized to obtain a good sampling of the $B - R$ color index as a function of time.

Based on our observation (see §2.3) of no sig-

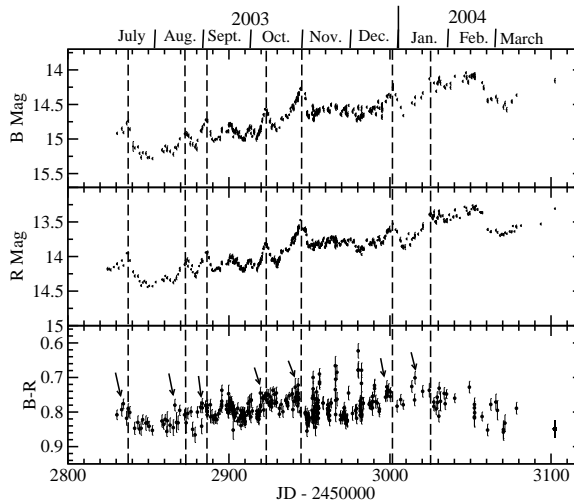


Fig. 12.— Light curve of the B and R magnitudes and the $B - R$ color index of 3C 66A over the duration of the entire campaign. While the B and R light curves are very well correlated, with no significant detection of a time delay, maxima of the spectral hardness (minima of $B - R$) systematically precede B and R outbursts by a few days.

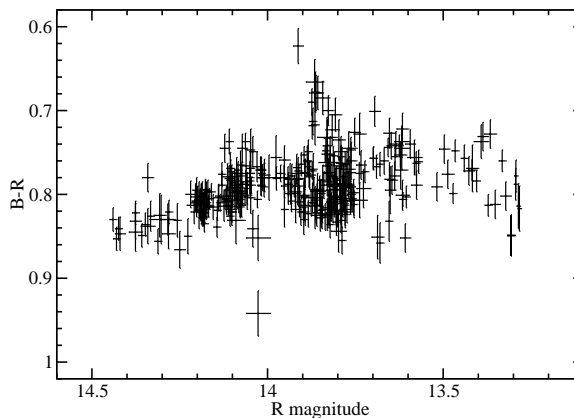


Fig. 13.— Optical hardness – intensity diagram for the complete data set over the entire duration of the campaign. While a positive hardness-intensity correlation seems to be present at low brightness, $R \gtrsim 14.0$, no clear correlation can be found in brighter states.

TABLE 5

99 % CONFIDENCE UPPER LIMITS ON THE VHE PHOTON FLUX FROM THE STACEE OBSERVATIONS FOR VARIOUS ASSUMPTIONS OF AN UNDERLYING INTRINSIC PHOTON SPECTRAL INDEX $\Gamma = \alpha + 1$

Γ	E_{thr} [GeV]	dN/dE at E_{thr} [photons $\text{m}^{-2} \text{s}^{-1} \text{GeV}^{-1}$]
2.0	200	5.23×10^{-9}
2.5	184	9.39×10^{-9}
3.0	150	2.26×10^{-8}
3.5	147	3.10×10^{-8}

TABLE 6

OBSERVATION LOG AND 99 % CONFIDENCE UPPER LIMITS ON THE INTEGRATED > 390 GeV PHOTON FLUX FROM THE WHIPPLE OBSERVATIONS OF 3C 66A, ASSUMING A CRAB-LIKE SPECTRUM.

Date	Start time [UTC]	On-Source Live Time [min.]	99.9 % UL [10^{-11} ergs $\text{cm}^{-2} \text{s}^{-1}$]
030927	10:57	27.73	2.05
030928	09:04	27.70	3.16
030929	08:16	27.75	2.73
031002	08:58	27.66	1.77
031002	09:27	27.73	2.35
031002	10:25	27.69	1.82
031023	06:58	27.55	6.19
031024	07:07	27.57	5.65
031028	06:40	27.55	6.35
031028	07:08	27.57	7.00
031029	06:41	27.57	6.62
031029	08:15	19.99	5.29
031030	06:27	27.61	4.39
031101	07:17	27.58	4.51
031125	05:49	27.55	6.32
031128	04:42	27.57	2.81
031214	03:06	27.62	4.87
031217	03:00	27.63	5.95
031217	04:08	27.54	5.23
031217	04:37	27.58	5.23
031217	05:05	27.55	6.71
031217	05:33	27.58	3.67
031220	03:38	27.63	2.60
031220	05:09	27.60	5.95
031220	06:07	27.66	4.45
031223	02:48	27.70	4.63
031223	04:01	27.71	4.03
031223	04:31	27.68	3.88
031223	04:59	27.70	2.94
031225	04:35	27.64	5.44
040113	02:17	27.58	5.23

nificant variability on time scale less than ~ 1 hr, we extracted B – R color indices on measurements of B and R magnitudes separated by less than 20 min. of each other. Fig. 12 shows a comparison of the light curves of the B and R magnitudes and the B – R color index. The figure reveals an interesting new result: While the B and R light curves are well correlated, with no significant detection of a time lag from a discrete correlation function analysis (see §4), maxima of the spectral hardness (i.e., minima of the value of B – R) seem to precede B and R band flux outbursts systematically by a few days. In other words, the optical spectra harden at the onset of a major outburst, and continue to soften as the flare progresses through both the rising and the decaying phase. However, Fig. 12 also indicates that the apparent lead time of the B – R hardness maximum varies within a range of a few days. This might be the reason that a cross-correlation analysis between the B – R index and the B or R light curves does not reveal a strong peak. In fact, the DCF between those time series does never exceed values of ~ 0.3 at all.

Very interesting and intriguing is also the B – R behaviour of the source around JD 2452955 – JD 2452995, where no major flux outbursts are observed, but several episodes of significant spectral hardening by $\Delta(B - R) \gtrsim 0.1$ (corresponding to spectral-index variations of $\Delta\alpha_{\text{opt}} \gtrsim 0.2$) are observed.

In Fig. 13 we have plotted the B – R index vs. R-band magnitude for the entire data set. The plot shows that there is a weak indication of a positive hardness-intensity correlation at low flux states with $R \gtrsim 14.0$. At higher flux levels, no correlation is apparent, which might be a consequence of the result found above, that the B – R hardness actually peaks during the rising phase of individual outbursts. This is in contrast with recent results of Vagnetti et al. (2003) who, on the basis of a smaller data set, have found a consistent trend of B – R hardening with increasing B-band flux, independent of the actual flux value.

The optical spectral hysteresis visible in our data is further illustrated in Fig. 14, where we have plotted the B – R vs. R hardness-intensity diagram for the example of one individual outburst on Nov. 1, 2003 (MJD 52944). The top panel shows the hardness-intensity diagram for the entire flare, which is then split up into the rising and

the decaying phase of the flare in the middle and lower panels, respectively. The figure illustrates that as the flare rises up to the peak R brightness, the spectrum already begins to soften significantly as $R \lesssim 13.6$. Similar trends are found for other optical flares as well. Possible physical interpretations of this trend, along with detailed modelling of the SED and spectral variability will be presented in a separate paper (Joshi & Böttcher 2005, in preparation).

4. Inter-band cross-correlations and time lags

In this section, we investigate cross-correlations between the measured light curves at different frequencies, within individual frequency bands as well as broadband correlations between different frequency bands. Because of relatively poor sampling of the radio and IR light curves, our searches for correlations between different radio and IR bands and between those wavelength bands with the optical ones on short time scales compared to the duration of our campaign did not return conclusive results. Also, in agreement with our non-detection of a periodicity on time scales of $\lesssim 50$ days, a discrete autocorrelation function (DACF Edelson & Krolik 1988) analysis of individual optical light curves did not return results beyond artificial “periodicities”. Such artifacts can be attributed to the quasi-periodic, uneven time coverage which results in spurious detections of periodicities at multiples of days and multiples of ~ 0.5 d (the time delay between the peak coverage from the heavily contributing observatories in Europe and in East Asia). A discrete autocorrelation function analysis of the R-band light curve also revealed secondary peaks at ± 4 days with a correlation coefficient close to 1.

The cleanest results of a DCF analysis are obviously expected for the most densely sampled light curves, which we obtained in the B and R bands. We performed DCFs between the R and B band light curves on a variety of time scales with a variety of binning intervals, ranging from 15 min. to 10 days. On intraday time scales, we find consistently a sharp peak at 0 delay with all bin sizes we used, which indicates no evidence for a time delay between variability patterns in the R and B band reaching their peak fluxes in each band.

The DCFs on short time scales are dominated by the artificial 0.5 d and 1 d periodicities mentioned above. The discrete correlation function between R and B band magnitudes on time scales of several days seems to indicate a strong correlation at $\tau \sim -4$ days, corresponding to a lead of the B vs. the R band. However, this might be a consequence of the probably artificial 4-day “periodicity” of the R-band light curve discussed in the previous paragraph, which prevents us from making any claim about the detection of a 4-day delay between the R and B band light curves on the basis of our DCF analysis.

5. Broad-band spectral energy distributions

From the various flux measurements described in detail in the previous sections, we can now compose contemporaneous spectral energy distributions (SEDs) of 3C 66A at various times during our campaign. Significant variability was only detected in the radio, IR, and optical bands. In those bands, we extracted SEDs for four epochs: During two major outbursts, around Nov. 1, 2003, and Dec. 28, 2003, a minor outburst around Oct. 1, 2003, as well as a rather quiescent state around Nov. 11, 2003. De-reddened optical and near-IR magnitudes were converted to fluxes using the zero-point normalizations of Bessel, Castelli, & Plez (1998). The resulting SEDs are plotted in Fig. 15. Due to the relatively poor sampling, radio and IR data were often not quite simultaneous with the optical spectra, which were extracted near the peaks of the individual outbursts mentioned above. In this case, the closest near-IR and radio data points were chosen. This led to time offsets between the optical and the radio data points of up to ~ 5 d. Given the relatively long time scale and moderate amplitude of variability at radio wavelengths, we are confident that this did not introduce serious distortions of the low-frequency SED.

In addition to the data taken during our 2003/2004 campaign, we have included historical X-ray measurements, to indicate the degree of X-ray variability observed in this source and the historical average GeV γ -ray flux measured by the EGRET instrument on-board the *Compton Gamma-Ray Observatory* from 5 observations

between Nov. 1991 and Sept. 1995 (Hartman et al. 1999).

The shape of the time-averaged optical (U)BVRI spectra, together with the very steep X-ray spectral index, indicates that the νF_ν peak of the synchrotron component of 3C 66A is typically located in the optical range. The shape of our best-fit *RXTE* spectrum provides strong evidence that the synchrotron component extends far into the X-ray regime and intersects the high-energy component in the time-averaged SED of 3C 66A at $\gtrsim 10$ keV during our core campaign period. Due to the lack of simultaneous GeV γ -ray coverage and of a firm detection at > 100 GeV, we can not make a precise statement concerning the level of γ -ray emission during our campaign. However, if the historical EGRET flux is representative also for the time of our campaign, then the total energy output in the low-frequency and the high-frequency components of the SED of 3C 66A are comparable, as is typical for the class of intermediate and low-frequency peaked BL Lac objects.

6. Generic parameter estimates

In this section, we discuss some general constraints on source parameters. We will first (§6.1) focus on parameter estimates using the spectral energy distribution and optical intraday variability measurements, most relevant to the innermost portion of the jet outflow, closest to the central engine. In §6.2, we will use the results of our VLBA observations to estimate parameters of the relativistic flow on parsec scales.

6.1. Parameters of the inner jet

From the minimum variability time scale of $\Delta t_{\min} \sim 2$ hr, we can estimate the size of the emitting region as $R \lesssim c D \Delta t_{\min}$, where $D = (\Gamma [1 - \beta_\Gamma \cos \theta_{\text{obs}}])^{-1}$, where Γ is the bulk Lorentz factor of the emitting region, $\beta_\Gamma c$ is the corresponding speed, and θ_{obs} is the observing angle. This yields $R \lesssim 2.2 \times 10^{15} \delta_1$ cm, where $\delta = 10 \delta_1 \sim 15$ as an estimate from the limits on superluminal motion and from previous modeling efforts, as mentioned in the introduction.

An estimate of the co-moving magnetic field can be found by assuming that the dominant portion of the time-averaged synchrotron spectrum is emitted by a quasi-equilibrium power-law spec-

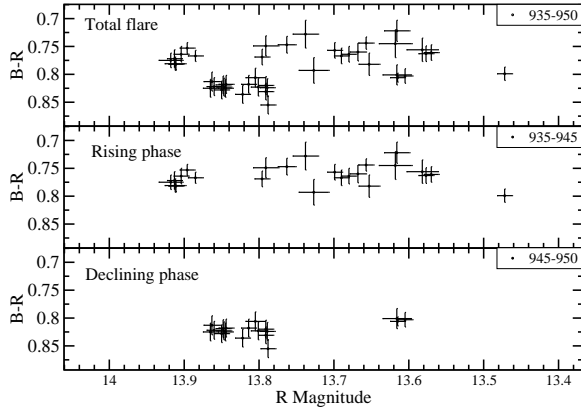


Fig. 14.— Optical hardness – intensity diagram for the flare around Nov. 1, 2003. The optical spectrum already begins to soften significantly while the R-band flux is still rising at $R \lesssim 13.6$.

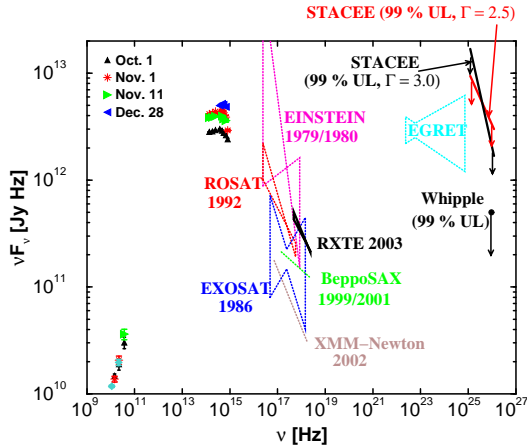


Fig. 15.— Time-averaged spectral energy distributions of 3C 66A at various epochs during the core campaign period in 2003. The turquoise diamonds indicate the average of the RATAN-600 measurements from Oct. 11 and 14, 2003. Historical soft X-ray spectra are plotted for comparison; the hard X-ray spectrum labelled “RXTE 2003” indicates the result of a power-law fit to the *RXTE* PCA observations of this campaign. The historical (non-contemporaneous) average of the 5 EGRET pointings on the source is also included for reference. All data that are not contemporaneous with our campaign are indicated by dotted curves.

trum of electrons with $N_e(\gamma) = n_0 V_B \gamma^{-p}$ for $\gamma_1 \leq \gamma \leq \gamma_2$; here, V_B is the co-moving blob volume. Based on the X-ray spectral index of $\alpha \approx 1.5$, we find a particle spectral index of $p \approx 4$. Since the synchrotron cooling time scale for X-ray emitting electrons might be much shorter than the dynamical time scale (see Eq. 3), the X-rays are likely to be produced by a cooled electron distribution. In this case, the index $p \approx 4$ corresponds to a distribution of electrons injected into the emission region with an original index $q \approx 3$. The normalization constant n_0 is related to the magnetic field through an equipartition parameter $e_B \equiv u_B/u_e$ (in the co-moving frame). Note that this equipartition parameter only refers to the energy density of the electrons, not accounting for a (possibly dominant) energy content of a hadronic matter component in the jet. Under these assumptions, the magnetic field can be estimated as described, e.g., in Böttcher et al. (2003). Taking the νF_ν peak synchrotron flux f_ϵ^{sy} at the dimensionless synchrotron peak energy ϵ_{sy} as $\sim 5 \times 10^{-11}$ ergs $\text{cm}^{-2} \text{s}^{-1}$ at $\epsilon_{\text{sy}} \approx 5 \times 10^{-6}$ and $R \approx 3.3 \times 10^{15}$ cm, we find

$$B_{e_B} = 4.4 \delta_1^{-1} e_B^{2/7} \text{ G}, \quad (1)$$

which yields $B_{e_B} \approx 2.9 e_B^{2/7} \text{ G}$ for $\delta = 15$.

We can further use this magnetic-field value to estimate the end points of the electron spectrum since the low-energy end, γ_1 might correspond to the νF_ν peak of the synchrotron spectrum, and the synchrotron high-energy cutoff corresponds to γ_2 . Generally, we find

$$\gamma \approx 3.1 \times 10^3 \nu_{15}^{1/2} \left(\frac{\delta}{15} \right)^{-1/2} \left(\frac{B}{2.9 \text{ G}} \right)^{-1/2}, \quad (2)$$

where ν_{15} is the characteristic synchrotron frequency in units of 10^{15} Hz. With our standard parameters, this yields $\gamma_1 \approx 3.1 \times 10^3$, and $\gamma_2 = 1.5 \times 10^5$, if the synchrotron cutoff occurs around 10 keV. We can also use this to estimate the synchrotron cooling time scale of electrons in the observer’s frame:

$$\tau_{\text{cool, sy}}^{\text{obs}} \approx 2.8 \times 10^3 \left(\frac{\delta}{15} \right)^{-1/2} \left(\frac{B}{2.9 \text{ G}} \right)^{-3/2} \nu_{15}^{-1/2} \text{ s}. \quad (3)$$

For optical frequencies, this yields observed cooling time scales of the order of ~ 2 hr, in agreement with the observed minimum variability time scale. This, however, raises an important caveat: The observed minimum variability time scale may, in fact, be a reflection of the electron cooling time scale rather than the dynamical time scale, as we had assumed when choosing our estimate for the source size R . For this reason, a more detailed future investigation of possible short-term variability at X-ray frequencies will be extremely important to resolve this issue. If X-ray variability on shorter time scales than ~ 2 hr is found, the emission region would then have to be more compact than the $R \sim 3 \times 10^{15}$ cm which we had estimated here, and X-ray spectral hysteresis patterns could arise. In contrast, if the X-ray variability time scale is found to be consistent with the optical one, then it would have to be dominated by the dynamical time scale and thus be largely achromatic. Thus, in that case no significant X-ray spectral hysteresis would be expected.

6.2. Parameters of the pc-scale outflow

In our analysis of the 22 GHz and 43 GHz VLBA maps of 3C 66A, we had found a rather smooth jet, with only one of the 6 Gaussian components (C1) showing evidence for superluminal motion of $\beta_{\text{app}} = (8.5 \pm 5.6) h^{-1}$. If we consider the measured speed of the component C1 to be close to the maximum as observed under the superluminal angle given by $\cos(\theta_{\text{obs}}^{\text{SL}}) = \beta_{\Gamma}$, we can estimate the minimum Lorentz factor and maximum angle between the jet and our line of sight. With $h = 0.7$ and by taking the lower limit of the $\beta_{\text{app}} \geq (8.5 - 5.6) h^{-1} = 2.9 h^{-1}$, we have a lower limit to the bulk Lorentz factor of $\Gamma \geq 4.3$ and an upper limit to the viewing angle of $\theta_{\text{obs}} \leq 27.2^\circ$. The large error in β_{app} results in very weak constraints on Γ and θ_{obs} , and they should be considered as very conservative estimates. Much more accurate values should be available after the analysis of all 9 epochs of the VLBA monitoring program (Savolainen et al. 2005, in preparation).

From the measured fluxes at 22 and 43 GHz, we have calculated the brightness temperatures along the jet. The largest brightness temperatures are found for the core, yielding lower limits of $T_b^{\text{core}} \sim 10^{11}$ K (see Tab. 2). Here, we have to mention the caveat that the errors for the size

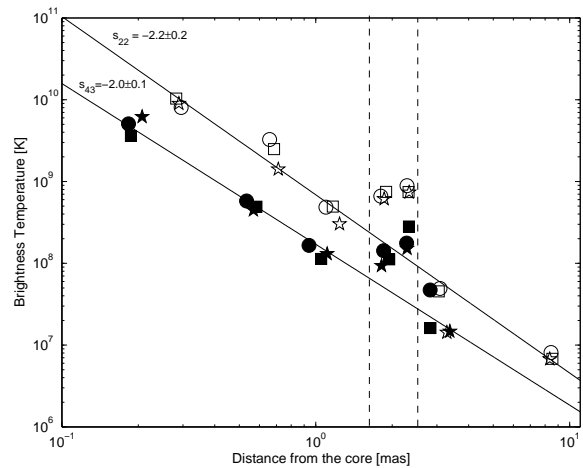


Fig. 16.— VLBA brightness temperatures as a function of distance from the core, at 22 GHz (filled symbols) and 43 GHz (open symbols), for the three epochs: 2003.78 (circles), 2003.83 (squares), 2004.08 (stars). The solid lines are our best-fit power-laws to the brightness-temperature profiles; the vertical dashed lines indicate the jet regions B2 and B3, where a significant deviation from the power-law profile is found, coincident with an apparent kink in the jet flow direction.

of the core are very difficult to estimate, since our model-fitting yields very asymmetric probability density distributions for the core size. Essentially, the data is also consistent with a point source core, so we can only give an upper limit to the core size. Thus, no upper limit to the core brightness temperature is available. Our calculated best-fit core brightness temperatures and corresponding lower limits are listed in Tab. 2 and can be compared with an equipartition brightness temperature (Readhead 1994) for 3C 66A of $T_{b,ep} = 6 * 10^{10}$ K. If the equipartition assumption holds, the minimum Doppler factor is around 2. The same result was obtained by Lähteenmäki & Valtaoja (1999) who used variability arguments to calculate the Doppler factor. Because we do not have upper limits for the brightness temperature, we cannot calculate a more precise value for the Doppler factor. However, if the core brightness temperatures calculated from the best model-fit values are not too far from the truth, the core Doppler factor probably lies somewhere between 2 and 15 with the average best-fit value of 6.

We have also calculated the brightness temperatures for components other than the core at both 22 and 43 GHz. In Fig. 16, the component brightness temperatures are plotted against the component distance from the core. The figure illustrates that the points form two well-defined power laws with a different scaling at different frequencies. All three epochs are included in the plot (and coded by colors). The brightness temperature gradient along the jet is well described by a power law $T_b \propto r^s$ with $s = -2$. There is an exception to the power law between 1.8 and 2.3 mas from the core, where the brightness temperature increases above the power law fit by a factor of 3 – 5. This takes place in the jet region B, where the jet is clearly bending. This brightening could be a result of a temporary increase of the Doppler factor caused by the bending of the jet towards our line of sight. An alternative interpretation could be given by impulsive particle acceleration in the region B by a standing shock wave caused by the interaction of the continuous, relativistic outflow with the observed kink.

The power law gradient of the brightness temperature along the jet suggests that 3C 66A exhibits a smooth pc-scale jet without any prominent particle acceleration sites (shocks) other than

the core and possibly the bend in region B. If we assume that the magnetic field B , the electron density N and the cross-sectional diameter D of the jet can also be described by power laws: $N \propto r^n$, $B \propto r^b$ and $D \propto r^d$, the brightness temperature is expected to fall with r as $T_b \propto r^s$ (with $s < 0$). If optically thin synchrotron emission and a constant Lorentz factor of the emitting electrons are assumed, $s = d + n + b(1 + \alpha)$, where α is the spectral index (see, e.g. Kadler et al. 2004). If we know the values of s , d and α , we can calculate the relationship between b and n , or, by assuming equipartition, the actual values of b and n . We know now that $s = -2$, and the average spectral index is $\langle \alpha_{22-43} \rangle = 0.15$.

We still need to find out the value of d . $d = 1$ would correspond to a constant opening angle (conical jet), but our imaging results allow us to estimate a more precise value from the data by plotting the component size versus distance from the core (see Fig. 17). Surprisingly, up to 2.5 mas from the core, the jet is very tightly collimated. A power-law fit to the observed correlation between the lateral jet size and distance from the core yields $d = 0.6$. After 2.5 mas, the jet opens up (or disrupts) and d becomes larger than 1. This might be another indication that the angle between the jet and our line of sight is changing along the jet. The observed opening angle of the jet, ψ_{obs} , is related to the intrinsic opening angle ψ_{int} , through $\psi_{obs} \approx \psi_{int} / \sin(\theta_{obs})$ for small values of ψ_{int} and θ_{obs} . Thus, the observed opening angle increases when the jet bends towards our line of sight, which is in accordance with the observed brightening of the jet in the region B.

If equipartition holds, we may assume $n = 2b$. Then, taking $d = 0.6$ yields $b = -0.8$ and $n = -1.7$. For the case of a conical jet ($d = 1$), we find $n = -1.9$ and $b = -1.0$. If the equipartition assumption holds, these results mean that in a conical jet, the magnetic field decays as $B \propto D^{-1}$, and in a collimated jet ($d = 0.6$), it decays as $B \propto D^{-1.3}$, implying a magnetic field that is predominantly transverse to the jet axis. This is in accordance with other observational results on the magnetic-field orientation in BL Lac objects in general (see, e.g. Gabuzda et al. 2004). A magnetic field being predominantly transverse to the jet agrees well with overall toroidal field configuration which is expected in Poynting flux dominated

(PFD) jet models. Another possibility for creating predominantly transverse magnetic field is the enhancement of the transverse magnetic field component by a series of shocks, but this seems to be less likely in this case, since we do not observe bright knots in the jet, but a rather smooth flow.

7. Summary

We have observed 3C 66A in a massive multi-wavelength monitoring campaign from July 2003 to April 2004. Monitoring observations were carried out at radio, infrared, optical, X-ray, and VHE γ -ray observations. The main observational results of our campaign are:

- In the optical, several outbursts by $\Delta m \sim 0.3 - 0.5$ over time scales of several days were observed.
- Optical intraday microvariability ($\Delta m \lesssim 0.05$) on time scales of $\Delta t_{\text{var}} \sim 2$ hr was detected.
- No clear evidence for periodicity was found, but a quasi-regular sequence of several major outbursts separated by $\sim 50 - 57$ d was identified.
- Large optical flares (on time scales of several days) seem to exhibit optical spectral hysteresis, with the B - R hardness peaking several days prior to the R- and B-band flux peaks.
- The 3 - 10 keV X-ray spectrum is best fitted with a single power-law with energy index $\alpha = 1.47 \pm 0.56$, indicating that the transition between the synchrotron and the high-energy components occurs at photon energies of $\gtrsim 10$ keV.
- Radio VLBA monitoring observations reveal a rather smooth jet with no clearly discernible knots or hot spots except for moderate brightening in the region B where the jet is bending.
- Decomposition of the VLBA radio structure into Gaussian components reveals superluminal motion only for one out of 6 components. Its apparent speed is $\beta_{\text{app}} = (8.5 \pm 5.6) h^{-1} = (12.1 \pm 8.0)$ for $h = 0.7$.

- The radio brightness temperature profile along the jet, along with its observed geometry, $D \propto r^{0.6}$, suggest a magnetic-field decay $B \propto D^{-1.3}$, indicating a predominantly perpendicular magnetic-field orientation.
- STACEE observations revealed a 2.2σ excess, which provided strict upper limits at $E_\gamma \gtrsim 150$ GeV. Additional VHE γ -ray limits at $E_\gamma > 390$ GeV resulted from simultaneous Whipple observations.
- The broadband SED of 3C 66A during our campaign suggests that the synchrotron component peaks in the optical and extends far into the X-ray regime, out to at least ~ 10 keV.
- The following parameters of the synchrotron emission region near the core can be estimated:

$$\begin{aligned}
 \delta &\approx 15 \\
 R &\approx 3.3 \times 10^{15} \text{ cm} \\
 B &\approx 2.9 \epsilon_B^{2/7} \text{ G} \\
 \gamma_1 &\approx 3.1 \times 10^3 \\
 \gamma_2 &\approx 1.5 \times 10^5 \\
 p &\approx 4
 \end{aligned} \tag{4}$$

- No X-ray variability was detectable by *RXTE* on a ~ 1 day time scale. Future X-ray observations with more sensitive X-ray detectors will be important to probe for rapid X-ray variability and X-ray spectral hysteresis in order to put more stringent constraints on the source size, the nature of the variability mechanism, and the composition and energetics of the emitting plasma in the jet.

The work of M. Böttcher and M. Joshi at Ohio University and of G. Fossati and I. A. Smith at Rice University was partially supported through NASA's *RXTE* guest observer program, award no. NNG 04GB13G. The European Institutes belonging to the ENIGMA collaboration acknowledge EC funding under contract HPRN-CT-2002-00321. The UMRAO is partially supported by funds from the NSF and from the University of Michigan's Department of Astronomy. The work of T. Savolainen was partly supported by the

Finnish Cultural Foundation. The St.-Petersburg group was supported by Federal Programs “Astronomy” (grant 40.022.1.1.1001) and “Integration” (grant B0029). J. H. Fan’s work is partially supported by the National 973 project (NKBRSF G19990754) of China, the National Science Fund for Distinguished Young Scholars (10125313). V. Hagen-Thorn and V. Larionov acknowledge support from the Russian Foundation for Basic Research, project 05-02-17562. The work at the Mt. Abu Infrared Observatory was supported by the DOS, Govt. of India. W. Cui and D. Able gratefully acknowledge support from the Department of Energy. The RATAN-600 observations were partly supported by the NASA JURRISS Program (grant W-19611) and the Russian Foundation for Basic Research (grant 05-02-17377).

REFERENCES

- Aharonian, F., et al., 2000, *A&A*, 353, 847
- Aharonian, F., et al., 2002, *A&A*, 384, L23
- Aller, M. F., Aller, D. H., & Hughes, P. A., 1994, in “Workshop on Intensive Monitoring of OJ 287”, eds. Kidger, M. R., & Takalo, L. O., *Tuorla Observatory Reports*, 174, 60
- Aller, H. D., Aller, M. F., Latimer, G. E., & Hodge, P. E., 1985, *ApJS*, 59, 513
- Bessel, M. S., Castelli, F., & Plez, B., 1998, *A&A*, 331, 231
- Bloom, S. D., et al., 1997, *ApJ*, 490, L145
- Böttcher, M., & Bloom, S. D., 2000, *AJ*, 119, 469
- Böttcher, M., 2002, in proc. “The Gamma-Ray Universe”, XXII Moriond Astrophysics Meeting, in press
- Böttcher, M., & Chiang, J., 2002, *ApJ*, 581, 127
- Böttcher, M., Mukherjee, R., & Reimer, A., 2002, *ApJ*, 581, 143
- Böttcher, M., et al., 2003, *ApJ*, 596, 847
- Bramel, D. A., et al., 2005, *ApJ*, submitted
- Bregman, J. N., et al., 1990, *ApJ*, 354, 574
- Carini, M. T., & Miller, H. R., 1991, *BAAS*, 23, 1420
- Carini, M. T., Miller, H. R., Noble, J. C., & Goodrich, B. D., 1992, *AJ*, 104, 15
- Catanese, M., et al., 1998, *ApJ*, 501, 616
- Chadwick, P. M., et al., 1999, *ApJ*, 513, 161
- Costamante, L., & Ghisellini, G., 2002, *A&A*, 384, 384, 56
- Croston, J. H., Hardcastle, M. J., Birkinshaw, M., & Worrall, D. M., 2003, *MNRAS*, 346, 1041
- de Jager, O., & Stecker, F. W., 2002, *ApJ*, 566, 738
- De Diego, J. A., Kidger, M. R., González-Pérez, N., & Lehto, H., 1997, *A&A*, 318, 331
- Dermer, C. D., & Atoyan, A. M., 2002, *ApJ*, 568, L81
- Edelson, R. A., & Krolik, J. H., 1988, *ApJ*, 333, 646
- Falcone, A. D., et al., 2004, *ApJ*, 613, 710
- Fan, J. H., & Lin, R. G., 1999, *ApJS*, 121, 131
- Fan, J. H., & Lin, R. G., 2000, *ApJ*, 537, 101
- Fossati, G., Maraschi, L., Celotti, A., Comastri, A., & Ghisellini, G., 1998, *MNRAS*, 299, 433
- Gabuzda, D. C., Eamonn, M., & Cronin, P., 2004, *MNRAS* 351, L89
- Georganopoulos, M., & Marscher, A. P., 1998, *ApJ*, 506, L11
- Ghisellini, G., Celotti, A., Fossati, G., Maraschi, L., & Comastri, A., 1998, *MNRAS*, 301, 451
- González-Pérez, J. N., Kidger, M. R., & Martín-Luis, F., 2001, *AJ*, 122, 2055
- Greisen, E. W., 1988, in “Acquisition, Processing, and Archiving of Astronomical Images”, ed. G. Longo & G. Sedmak (Napoli: Osservatorio Astronomico di Capodimonte), 125
- Hartman, R. C., et al., 1999, *ApJS*, 123, 79
- Hillas, A. M., et al., 1998, *ApJ*, 503, 744
- Holder, J., et al., 2003, *ApJ*, 583, L9

- Homan, D. C., Ojha, R., Wardle, J. F. C., Roberts, D. H., Aller, M. F., Aller, H. D., & Hughes, P. A., 2001, *ApJ*, 549, 840
- Horan, D., et al., 2002, *ApJ*, 571, 753
- Horan, D., et al., 2004, *ApJ*, 603, 51
- Jorstad, S. G., Marscher, A. P., Mattox, J. R., Wehrle, A. E., Bloom, S. D., & Yurchenko, A. V., 2001, *ApJS*, 134, 181
- Jorstad, S. G., et al., 2005, *ApJ*, submitted (astro-ph/0502501)
- Kadler, M., Ros, E., Lobanov, A. P., Falcke, H., & Zensus, J. A., 2004, *A&A*, 426, 481
- Kataoka, J., Takahashi, T., Makino, F., Inoue, S., Madejski, G. M., Tashiro, M., Urry, C. M., & Kubo, H., 2000, *ApJ*, 528, 243
- Kirk, J. G., Rieger, F. M., & Mastichiadis, A., 1998, *A&A*, 333, 452
- Kovalev, Y. Y., et al., 1999, *A&AS*, 139, 545
- Krawczynski, H., Coppi, P. S., & Aharonian, F. A., 2002, *MNRAS*, 336, 721
- Kusunose, M., Takahara, F., & Li, H., 2000, *ApJ*, 536, 299
- Lähtenmäki, A., & Valtaoja, E., 1999, *ApJ*, 521, 493
- Lanzetta, K. M., Turnshek, D. A., & Sandoval, J., 1993, *ApJS*, 84, 109
- Lainela, M., et al., 1999, *ApJ*, 521, 561
- Li, H., & Kusunose, M., 2000, *ApJ*, 536, 729
- Lovell, J., 2000: “Difwrap: A Graphical User Interface for Error Analysis in Difmap.” In “Astrophysical Phenomena Revealed by Space VLBI”, eds. H. Hirabayashi, P. G. Edwards, & D. W. Murphy, Institute of Space and Astronautical Science, 301
- Mattox, J. R., Hartman, R. C., & Reimer, O., 2001, *ApJS*, 135, 155
- Miller, J. S., French, H. B., & Hawley, S. A., 1978, in *Pittsburgh Conference on BL Lac Objects*, ed. A. M. Wolfe (Pittsburgh: Univ. Pittsburgh), p. 176
- Miller, H. R., & McGimsey, B. Q., 1978, *ApJ*, 220, 19
- Miller, H. R., Carini, M. T., & Goodrich, B. D., 1989, *Nature*, 337, 627
- Mücke, A., & Protheroe, R. J., 2001, *Astropart. Phys.*, 15, 121
- Mücke, A., Protheroe, R. J., Engel, R., Rachen, J. P., & Stanev, T., 2003, *Astropart. Phys.*, 18, 593
- Neshpor, Yu. I., Stepanyan, A. A., Kalekin, O. R., Fomin, V. P., Chalenko, N. N., & Shitov, V. G., 1998, *Astron. Lett.*, 24, 2, 134
- Neshpor, Yu. I., Stepanyan, A. A., Kalekin, O. R., Zhogolev, N. A., Fomin, V. P., Chalenko, N. N., & Shitov, V. G., 2000, *Astronomy Reports*, 44, 10, 641
- Neshpor, Yu. I., Chalenko, N. N., Stepanian, A. A., Kalekin, O. R., Jogolev, N. A., Fomin, V. P., & Shitov, V. G., 2001, *Astronomy Reports*, 45, 249
- Perri, M., Massaro, E., Giommi, P., Capalbi, M., Nesci, R., Tagliaferri, G., Ghisellini, G., Ravasio, M., & Miller, H. R., 2003, *A&A*, 407, 453
- Price, R., Gower, A. C., Hutchings, J. B., Talon, S., Duncan, D., & Ross, G., 1993, *ApJS*, 86, 365
- Punch, M., et al., 1992, *Nature*, 358, 477
- Quinn, J., et al., *ApJ*, 456, L83
- Raiteri, C. M., et al., 2001, *A&A*, 377, 396
- Raiteri, C. M., et al., 2005, *A&A*, in press
- Readhead, A. C. S., 1994, *ApJ*, 426, 51
- Rieger, F. M., 2004, *ApJ*, 615, L5
- Ryter, C. E., 1996, *Astrophys. & Space Sci.*, 236, 285
- Sambruna, R. M., Barr, P., Giommi, P., Maraschi, L., Tagliaferri, G., & Treves, A., 1994, *ApJ*, 95, 371
- Sambruna, R., et al., 1999, *ApJ*, 515, 140

- Schlegel, D. J., Finkbeiner, D. P., & Davis, M., 1998, *ApJ*, 500, 525
- Shepherd, M. C., 1997, in *ASP Conf. Ser.*, 125, “Astronomical Data Analysis Software and Systems VI”, ed. G. Hunt & H. E. Payne (San Francisco: ASP), 77
- Sikora, M., Madejski, G., Moderski, R., & Poutanen, J., 1997, *ApJ*, 484, 108
- Sikora, M., & Madejski, G., 2000, *ApJ*, 534, 109
- Speziali, R., & Natali, G., 1998, *A&A*, 339, 382
- Takahashi, T., et al., 1996, *ApJ*, 470, L89
- Takalo, L. O., Kidger, M. R., de Diego, J. A., Sillanpää, A., & Nilsson, K., 1992, *AJ*, 104, 40
- Takalo, L. O., et al., 1996, *A&AS*, 120, 313
- Taylor, G. B., Vermeulen, R. C., Readhead, A. C. S., Pearson, T. J., Henstock, D. R., & Wilkinson, P. N., 1996, *ApJS*, 107, 37
- Teräsranta, H., et al., 1998, *A&AS*, 132, 305
- Vagnetti, F., Trevese, D., & Nesci, R., 2003, *ApJ*, 590, 123
- Villata, M., et al., 2000, *A&A*, 363, 108
- Villata, M., et al., 2002, *A&A*, 390, 407
- Villata, M., et al., 2004a, *A&A*, 421, 103
- Villata, M., et al., 2004b, *A&A*, 424, 497
- Walker, M. A., 1998, *MNRAS*, 294, 307
- Weekes, T. C., et al., 2002, *Astropart. Phys.*, 17, 221
- Wills, B. J., & Wills, D., 1974, *ApJ*, 190, L97
- Worrall, D. M., Puschell, J. J., Rodriguez-Espinosa, J. M., Bruhweiler, F. C., Miller, H. R., Aller, M. F., & Aller, H. D., 1984, *ApJ*, 286, 711
- Worrall, D. M., & Wilkes, B. J., 1990, *ApJ*, 360, 396
- Wu, J. H., & Urry, C. M., 2002, *ApJ*, 579, 530
- Wurtz, R., Stocke, J. T., & Yee, H. K. C., 1996, *ApJS*, 103, 109
- Xie, G. Z., Li, K. H., Liu, F. K., Wu, J. X., Fan, J. H., Zhu, Y. Y., & Cheng, F. Z., 1992, *ApJS*, 80, 683

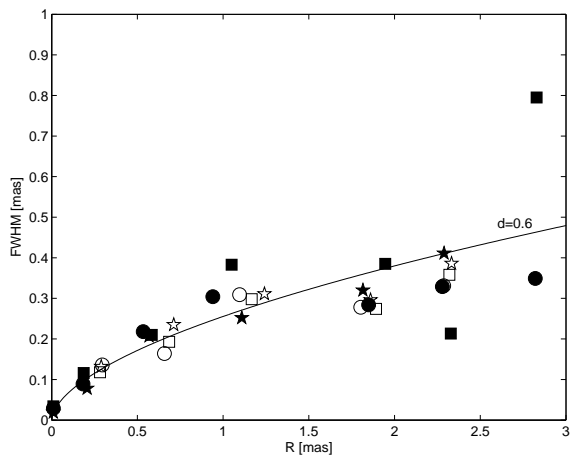


Fig. 17.— Transverse diameter D (FWHM of Gaussian component fits) of the jet as a function of distance from the core for the inner 3 mas. The symbols are the same as in Fig. 16. The solid curve illustrates the best-fit power law $D \propto r^d$, which yields $d = 0.6$.